Lattice dynamics, crystal-field excitations, and quadrupolar fluctuations of $YbRu_2Ge_2$

Mai Ye,[1,*] E. W. Rosenberg,[2] I. R. Fisher,[2] and G. Blumberg[1,3,†]
[1]*Department of Physics and Astronomy, Rutgers University, Piscataway, New Jersey 08854, USA*
[2]*Department of Applied Physics, Stanford University, California 94305, USA*
[3]*Laboratory of Chemical Physics, National Institute of Chemical Physics and Biophysics, 12618 Tallinn, Estonia*

(Received 7 February 2019; revised manuscript received 2 May 2019; published 3 June 2019)

We employ polarization-resolved Raman scattering spectroscopy to study ferroquadrupolar (FQ) fluctuations and crystal-field (CF) excitations in the $YbRu_2Ge_2$ heavy-fermion metal with FQ transition at $T_Q = 10\,\mathrm{K}$. We demonstrate that the electronic static Raman susceptibilities in quadrupolar symmetry channels exhibit nearly Curie law behavior and that the electron-lattice coupling is essential for the FQ transition at T_Q. We establish the CF level scheme of the Yb^{3+} ground state $^2F_{7/2}$ multiplet. We study the lattice dynamics and demonstrate coupling between CF transitions and phonon modes.

DOI: 10.1103/PhysRevB.99.235104

I. INTRODUCTION

Multipolar interactions and related ordering phenomena have attracted great interest because, unlike commonly known long-range orders of electric or magnetic dipole moments, multipoles are often related to more exotic phases which are difficult to probe directly by conventional methods [1,2]. For systematic investigation of the collective behavior of multipole moments, f-electron systems are suitable choices since the strong coupling between spin and orbital degrees of freedom of f electrons facilitates multipole formation. Indeed, the actinide dioxides with $5f$ electrons exhibit a variety of multipolar ordering phenomena [2]. For lanthanides with $4f$ electrons, multipolar, especially quadrupolar, orders have been discovered for different systems [3–7].

$YbRu_2Ge_2$, a heavy-fermion metal with tetragonal structure (space group $I4/mmm$, No. 139; point group D_{4h}), has been suggested to hold a ferroquadrupolar (FQ) order at low temperature [8–15]. It undergoes a second-order phase transition at $T_Q = 10\,\mathrm{K}$, before entering into an antiferromagnetic (AFM) phase below $T_{N1} = 6.5\,\mathrm{K}$ [8,13]. At $T_{N2} = 5.5\,\mathrm{K}$, there may exist a small change in the magnetic structure [11,13]. Early studies show that the transition at T_Q is not magnetic, and T_Q increases when magnetic field is applied along the easy direction [8,13]. This behavior at T_Q is similar to that of $TmAu_2$ at its FQ ordering temperature [16], hence suggesting a FQ phase in $YbRu_2Ge_2$. The existence of a FQ order is further supported by recent elastoresistivity studies in which above T_Q the elastoresistivity in the quadrupolar symmetry channels displays a Curie-Weiss behavior [14]. Below T_Q, an orthorhombic structural distortion is observed by x-ray diffraction, which confirms that the FQ state breaks B_{1g} $(x^2 - y^2)$ symmetry [14].

The FQ order, namely, the ordering of Yb^{3+} $4f$-electron charge distribution at zero wave vector, can be probed indirectly by studying the lattice dynamics and crystal-field (CF) excitations. In a FQ arrangement, aligned charge quadrupoles uniformly distort the lattice via a coupling between the quadrupole moment and the strain field with the same symmetry. The induced distortion reduces the point-group symmetry of the lattice system, splitting degenerate phonon modes; the distortion also modifies the energy and lifetime of the phonon modes of the same symmetry. Such anomalies can be revealed by investigating the phonon spectra. In addition, the quadrupolar moments are carried by the CF ground state of Yb^{3+}. The tetragonal CF potential splits the $^2F_{7/2}$ ground multiplet into two Γ_6 and two Γ_7 Kramers doublets. The magnetic entropy right above T_Q is nearly $R\ln 4$ [8], suggesting that the CF ground state is a quasiquartet consisting of two quasidegenerate Kramers doublets. The quasiquartet ground state was recently confirmed by angle-resolved photoemission spectroscopy studies [15]. This quasiquartet near degeneracy is essential for forming a quadrupolar ground state and deserves detailed study.

Raman spectroscopy is a conventional tool for studying phonon modes [17] and CF excitations [18]. Here we study the lattice dynamics, low-energy quadrupole fluctuations, and CF excitations in $YbRu_2Ge_2$. We assign four Raman-active phonon modes and reveal an anomalous intensity enhancement of two phonon modes on cooling. The three CF transitions within the $^2F_{7/2}$ ground multiplet are identified, and a CF level scheme is in turn established. We demonstrate that the low-energy Raman response undergoes remarkable enhancement on cooling towards T_Q and that the static electronic Raman susceptibility in the corresponding quadrupole channels follows nearly perfect Curie behavior, signifying that the relatively strong coupling to the lattice in the B_{1g}-symmetry channel enhances by about 10 K the vanishingly small electronic Weiss temperature to the FQ transition temperature T_Q.

II. EXPERIMENT

Single crystals of $YbRu_2Ge_2$ were grown using the flux method; details of the growth can be found in Ref. [14].

*mye@physics.rutgers.edu
†girsh@physics.rutgers.edu

TABLE I. The relationship between the scattering geometries and the symmetry channels. For scattering geometry E_iE_s, E_i, and E_s are the polarizations of incident and scattered light. X, Y, X′, Y′, and Z are the [100], [010], [110], [1$\bar{1}$0], and [001] crystallographic directions; R and L are right- and left-circular polarizations. A_{1g}, A_{2g}, B_{1g}, B_{2g}, and E_g are the irreducible representations of the D_{4h} group.

Scattering geometry	Symmetry channel
XX	$A_{1g} + B_{1g}$
XY	$A_{2g} + B_{2g}$
X′X′	$A_{1g} + B_{2g}$
X′Y′	$A_{2g} + B_{1g}$
XZ	E_g
RR	$A_{1g} + A_{2g}$
RL	$B_{1g} + B_{2g}$

Two samples were used in this study: one was cleaved in ambient conditions to expose its xy crystallographic plane; the other had a clean as-grown xz crystallographic plane. The xy crystallographic plane was examined under a Nomarski microscope to find an about $200 \times 200\,\mu m^2$ strain-free area.

Raman scattering measurements were performed in a quasibackscattering geometry from the sample placed in a continuous-helium-gas-flow cryostat. We used 476.2-, 647.1-, and 752.5-nm lines from a Kr^+ ion laser for excitation. Incident light with no more than 14-mW power was focused on a $50 \times 100\,\mu m^2$ spot. Particularly, for measurements below 10 K, the power of the incident light was reduced to 2 mW. The temperatures reported in this paper were corrected for laser heating, which was estimated to be 0.75 ± 0.25 K/mW [19].

Seven polarization configurations were employed to probe excitations in different symmetry channels. The relationship between the scattering geometries and the symmetry channels [20] is given in Table I.

We used a custom triple-grating spectrometer with a liquid-nitrogen-cooled charge-coupled device detector for analysis and collection of the scattered light. The data were corrected for the spectral response of the system. The measured secondary-emission intensity $I(\omega, T)$ is related to the Raman response $\chi''(\omega, T)$ by $I(\omega, T) = [1 + n(\omega, T)]\chi''(\omega, T) + L(\omega, T)$, where n is the Bose factor, ω is energy, and T is temperature. $L(\omega, T)$ represents the far tail of photoluminescence, which in the narrow spectral window of interest was approximated by a linear frequency dependence.

III. RESULTS AND DISCUSSION

A. Lattice dynamics

The spectra of phonon modes are presented in Fig. 1. By group theory, four Raman-active optical phonon modes are expected for the $YbRu_2Ge_2$ structure: $A_{1g} \oplus B_{1g} \oplus 2E_g$. The A_{1g} and B_{1g} modes are accessible in XX geometry, and E_g modes are accessible in XZ geometry. The phonon energies at 13 K are tabulated in Table II.

In Fig. 2 we show the temperature dependence of the spectral parameters (energy, FWHM, and integrated intensity) of the phonon modes. The spectral parameters were obtained

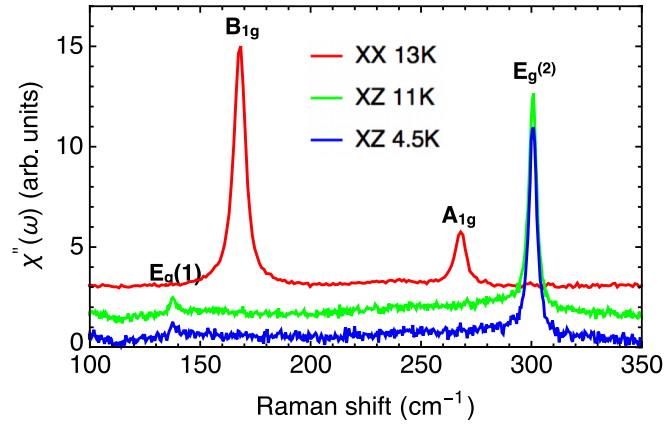

FIG. 1. Raman response $\chi''(\omega, T)$ of four Raman-active optical phonon modes at low temperature measured with the 647.1-nm excitation. The XX and XZ spectra are offset by 1.5 and 3 arbitrary units (arb. units), respectively. The spectral resolution is 1.0 cm^{-1}.

by fitting the measured spectral peaks with Lorentzian line shapes.

The temperature dependence of both frequency and FWHM of the phonon modes [Figs. 2(a) and 2(b)] is in accordance with a simple model assuming anharmonic decay into two phonons with identical frequencies and opposite momenta [21,22]:

$$\omega(T) = \omega_0 - \omega_2\left[1 + \frac{2}{e^{\hbar\omega_0/2k_BT} - 1}\right], \quad (1)$$

and

$$\Gamma(T) = \Gamma_0 + \Gamma_2\left[1 + \frac{2}{e^{\hbar\omega_0/2k_BT} - 1}\right]. \quad (2)$$

The fitting results are summarized in Table III. Small deviations between the measured energy and the fitting curve for the B_{1g} mode could be due to additional decay channels, for example, decay into one acoustic mode and one optical mode.

The integrated intensity of the A_{1g} and $E_g^{(2)}$ phonon modes increases more than 50% on cooling, in contrast to the behavior of the B_{1g} phonon mode, whose integrated intensity is nearly temperature independent [Fig. 2(c)]. The increase of the integrated intensity on cooling suggests a coupling

TABLE II. Summary of the energy of the phonon and crystal-field (CF) modes. The coupled CF and phonon modes are labeled by "(c)." Results of this work are compared to the inelastic neutron scattering (INS) study [38]. Units are cm^{-1}.

Mode	This work	INS
$\Gamma_6^{(1)} \rightarrow \Gamma_7^{(1)}$	2	
$\Gamma_6^{(1)} \rightarrow \Gamma_7^{(2)}$	95	89
$\Gamma_6^{(1)} \rightarrow \Gamma_6^{(2)}$ (c)	239	
A_{1g} (c)	268	260
B_{1g}	168	170
$E_g^{(1)}$	138	
$E_g^{(2)}$ (c)	301	

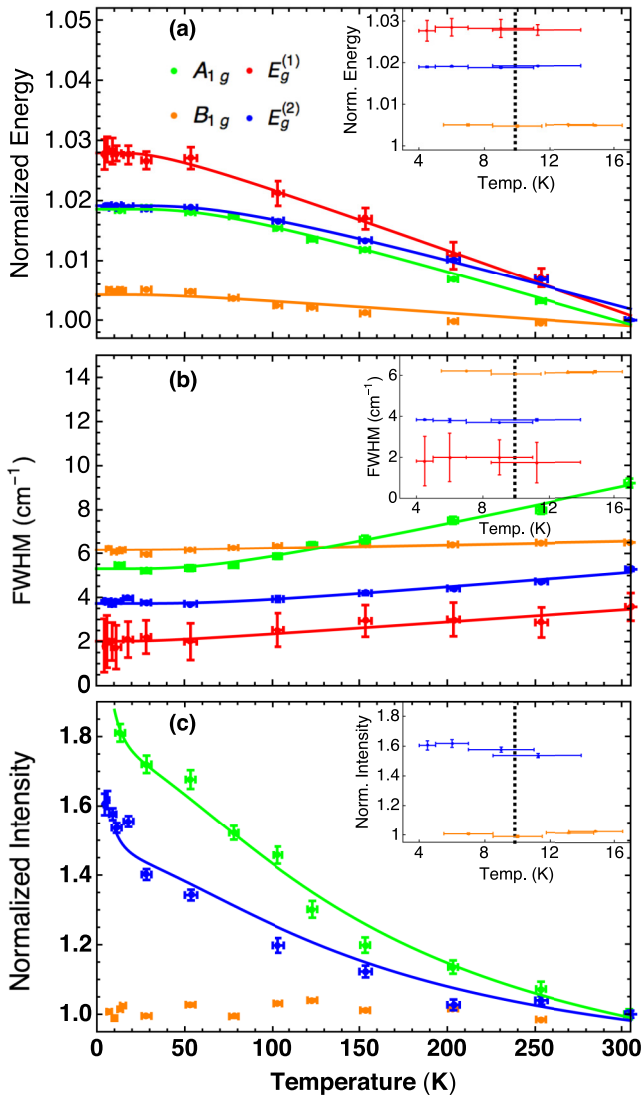

FIG. 2. Temperature dependence of (a) the energy, (b) the FWHM, and (c) the integrated intensity of the Raman-active optical phonon modes. The energy and integrated intensity are normalized to their respective values at 304 K. The integrated intensity of the very weak $E_g^{(1)}$ phonon mode is not shown. The solid lines in (a) and (b) represent the fits to the anharmonic decay model [21,22], while the solid lines in (c) represent the fits to Eq. (14). Insets: close-ups of the low-temperature data points showing how the physical properties change across the phase-transition temperature $T_Q = 10$ K. The dashed line in the insets indicate T_Q. The vertical error bars are derived from Lorentzian fits and represent one standard deviation; the horizontal error bars are derived from the uncertainty of laser heating estimation.

of a CF transition to these two phonon modes [23]. This coupling is enhanced when the energies of the CF splitting and the phonon modes are close. Indeed, such a CF excitation, 239 cm^{-1} at 13 K, exists. The mechanism of this coupling will be discussed in Sec. III C 2 below.

Because the FQ order parameter is of B_{1g} symmetry [14], the energy and lifetime of the B_{1g} phonon mode are expected to exhibit anomalies across T_Q due to electron-phonon coupling. Moreover, breaking of the fourfold rotational symmetry

TABLE III. The fitting parameters for the energy and FWHM of the four Raman-active optical phonon modes.

Mode	ω_0	ω_2	Γ_0	Γ_2
$E_g^{(1)}$	138.4 ± 0.1	0.70 ± 0.03	1.7 ± 0.5	0.3 ± 0.1
B_{1g}	167.92 ± 0.01	0.212 ± 0.002	6.08 ± 0.02	0.094 ± 0.005
A_{1g}	270.15 ± 0.04	2.27 ± 0.02	3.6 ± 0.1	1.71 ± 0.07
$E_g^{(2)}$	303.32 ± 0.02	2.67 ± 0.01	2.98 ± 0.05	0.75 ± 0.03

should split the two E_g phonon modes [24]. However, as shown in the insets of Fig. 2, B_{1g} and E_g phonon modes do not exhibit a significant anomaly across T_Q. E_g phonon modes do not show notable splitting at 4.5 K either (Fig. 1). The splitting of the $E_g^{(1)}$ phonon mode is challenging to observe due to its weak intensity. Because the FWHM of the $E_g^{(2)}$ phonon mode is 4 cm^{-1} at 4.5 K, we set the upper limit of the splitting of the E_g phonon modes to be about 4 cm^{-1} at 4.5 K.

B. Quadrupolar fluctuations

In the tetragonal phase above T_Q, the fourfold rotational symmetry along the z axis is preserved, and the CF ground state supports no static xy-plane quadrupole moment. However, dynamical quadrupolar fluctuations with zero time average quadrupolar moment are allowed [25].

In Fig. 3 we show the spectra of low-energy quadrupolar fluctuations. They are present in RL geometry but absent in RR geometry [Fig. 3(a)]. By group theory, the absence of A_{1g} and A_{2g} components indicates that the CF ground state is a quasiquartet composed of one Γ_6 doublet and one Γ_7 doublet.

The static Raman susceptibility $\chi_\mu(0, T)$ in the symmetry channel μ ($\mu = B_{1g}$ or B_{2g}) can be obtained from the Raman response $\chi''_\mu(\omega, T)$ by virtue of the Kramers-Kronig relation [26,27]:

$$\chi_\mu(0, T) = \frac{2}{\pi} \int_0^{\omega_{\max}} \frac{\chi''_\mu(\omega, T)}{\omega} d\omega, \tag{3}$$

in which we choose the upper cutoff for the spectra of fluctuations at $\omega_{\max} = 40$ cm^{-1} (see Fig. 3).

We use the Drude line shape

$$\chi''_\mu(\omega, T) \propto \frac{Q_\mu^2 \omega}{\omega^2 + \gamma_\mu^2} \tag{4}$$

to extrapolate the Raman response below the instrumental cutoff 5 cm^{-1}. In Eq. (4), Q_μ is the magnitude of the quadrupolar moment, and γ_μ reflects the decay rate. In the Raman scattering process light couples to the system's charge quadrupole moment.

Theoretically, the low-energy Raman response in the quadrupolar channels contains both the lattice and the electronic contributions [26,27]. However, the energy of lattice fluctuations is much lower than the instrumental cutoff (5 cm^{-1}), and Eq. (4) takes into account only the electronic contribution. Thus, only electronic quadrupole fluctuations are included in the derived susceptibility $\chi_\mu(0, T)$.

The obtained temperature dependence of the static electronic Raman susceptibilities for both B_{1g} and B_{2g} quadrupole channels is shown in Fig. 4. The static Raman susceptibility

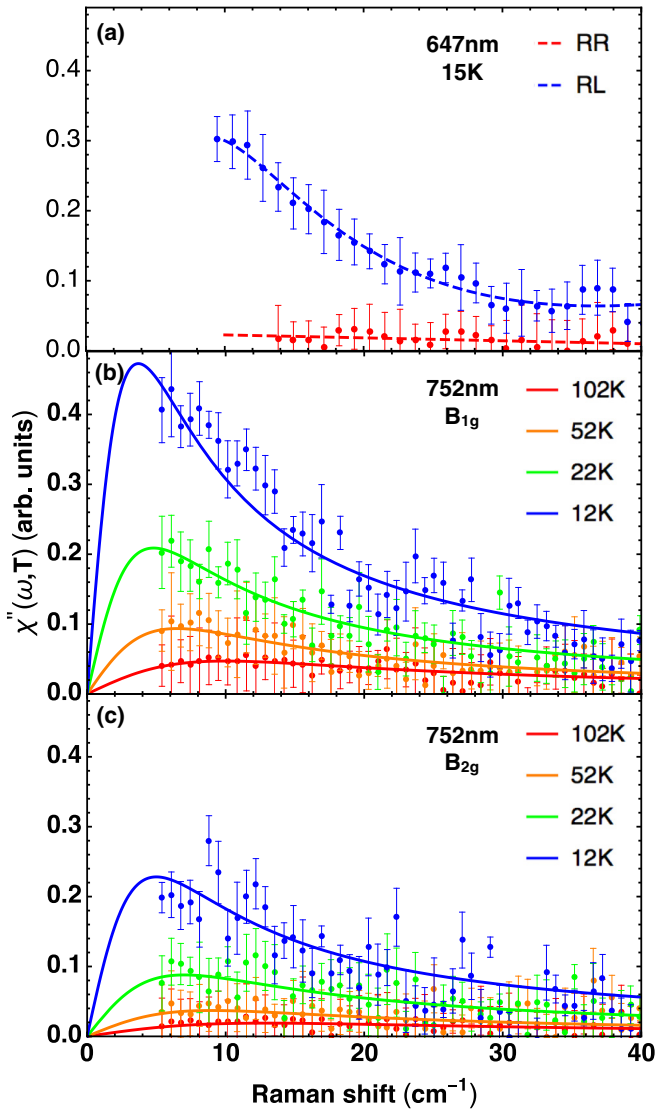

FIG. 3. Raman response $\chi''(\omega, T)$ for (a) RR and RL scattering geometries with the 647.1-nm excitation, (b) X′Y′ geometry with the 752.5-nm excitation, and (c) XY geometry with the 752.5-nm excitation. The solid lines are Drude fits, Eq. (4). The error bars represent one standard deviation.

$\chi_\mu(0, T)$ obeys Curie-Weiss temperature dependence

$$\chi_\mu(0, T) \propto \frac{Q_\mu^2}{T - T_W^\mu}, \tag{5}$$

where T_W^μ is the Weiss temperature:

$$T_W^\mu = \kappa_\mu Q_\mu^2, \tag{6}$$

in which κ_μ measures the strength of the electronic intersite quadrupolar interactions.

By fitting the data, the ratio of $Q_{B_{1g}}$ to $Q_{B_{2g}}$ is determined to be nearly 1.4. The derived Weiss temperatures are $T_W^{B_{1g}} \sim -2$ and $T_W^{B_{2g}} \sim +2$ K [28]. The nearly exact Curie law is not surprising because both direct exchange and superexchange between local quadrupolar moments are expected to be vanishingly weak due to the compactness of the f orbitals.

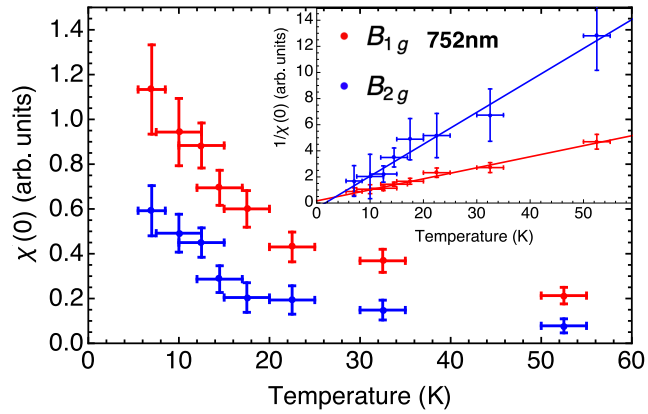

FIG. 4. Temperature dependence of the static electronic Raman susceptibility $\chi(0, T)$ for B_{1g} (red) and B_{2g} (blue) quadrupole channels derived from the Raman response shown in Fig. 3. Inset: temperature dependence of $1/\chi(0, T)$. The solid lines are Curie-Weiss fits, Eq. (5). The vertical error bars represent one standard deviation; the horizontal ones are derived from the uncertainty of the laser heating estimation.

Although itinerant electrons provide effective coupling between the local magnetic dipole moments at Yb^{3+} sites and the resulting Ruderman-Kittel-Kasuya-Yosida interaction [29] leads to AFM order below $T_{N1} = 6.5$ K, these itinerant electrons do not provide a significant effective coupling between the local electric quadrupole moments at Yb^{3+} sites.

The true B_{1g}-symmetry FQ order develops at $T_Q = 10$ K [14], about 10 K above the Weiss temperature $T_W^{B_{1g}}$. Because YRu_2Ge_2, the nonmagnetic analog of the same structure, has no orthorhombic transition [14,30], the quadrupolar fluctuations of the $YbRu_2Ge_2$ lattice themselves should have little tendency towards a structural instability. Nevertheless, coupling between the lattice strain fields and the local electronic quadrupole moments of the same symmetry enhances the transition temperature [26,27,31,32]:

$$T_Q^\mu = T_W^\mu + (\lambda_\mu^2/C_\mu)Q_\mu^2 = (\kappa_\mu + \lambda_\mu^2/C_\mu)Q_\mu^2, \tag{7}$$

where λ_μ measures the coupling between the local charge quadrupole moments on Yb^{3+} sites and the lattice strain fields and C_μ is the symmetrized elastic constant, which is $(C_{11}–C_{12})/2$ for the B_{1g} channel or C_{66} for the B_{2g} channel [33]. The true quadrupolar transition temperature T_Q equals the largest of two T_Q^μ. Because the FQ order in $YbRu_2Ge_2$ has B_{1g} symmetry, $T_Q^{B_{1g}} = T_Q$, and nonrealized $T_Q^{B_{2g}} < T_Q$.

Tuning an additional parameter (magnetic field, pressure, or doping, for instance) may affect the electron-lattice coupling and induce a transition from B_{1g} FQ ordering to B_{2g} FQ ordering. Indeed, although T_Q stays constant up to application of 9 GPa of pressure with zero magnetic field [11] and increases with in-plane magnetic field at ambient pressure [8], experimental results do show suppression of T_Q by Si [12] or Rh [15] doping and by applying magnetic field under 1.23-GPa pressure [11]. These results suggest a competition between B_{1g}- and B_{2g}-symmetry FQ order.

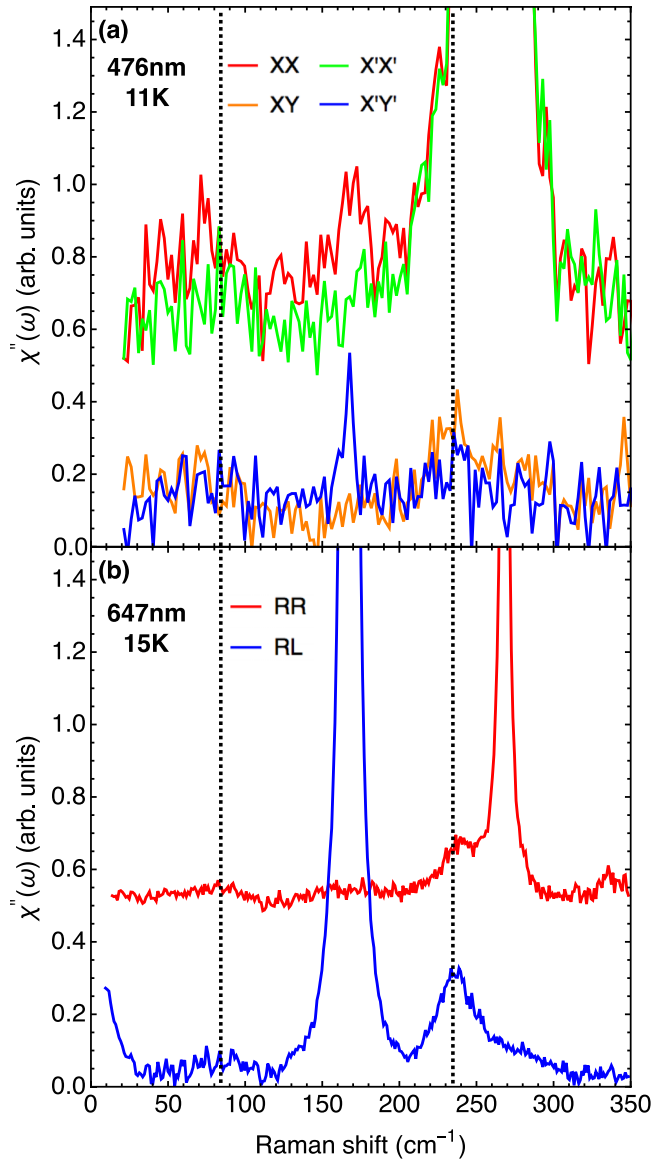

FIG. 5. Raman response $\chi''(\omega, T)$ of the CF excitations from the quasiquartet to the remaining two CF levels at low temperature. The dashed lines indicate the position of the two CF transitions. (a) The spectra for four linear polarizations measured at 11 K with the 476.2-nm excitation. The XX and X′X′ spectra are offset by 0.5 arbitrary units (arb. units). The spectral resolution is 3.5 cm^{-1}. (b) The spectra for two circular polarizations measured at 15 K with the 647.1 nm excitation. The RR spectrum is offset by 0.5 arbitrary unit. The spectral resolution is 2.5 cm^{-1}.

C. Crystal-field excitations

Within the $^2F_{7/2}$ multiplet, there are three CF excitations corresponding to transitions from the CF ground state to the three CF excited states. From group-theoretical considerations [34], the CF transitions between levels of the same symmetry (i.e., $\Gamma_6 \rightarrow \Gamma_6$ or $\Gamma_7 \rightarrow \Gamma_7$) contain A_{1g}, A_{2g}, and E_g representations, whereas those between levels of different symmetries (i.e., $\Gamma_6 \rightarrow \Gamma_7$ or $\Gamma_7 \rightarrow \Gamma_6$) contain B_{1g}-, B_{2g}-, and E_g-symmetry representations. The Raman intensities in different symmetry channels may vary due to the matrix element effect.

The lowest-energy CF transition, namely, the transition between the two quasidegenerate Kramers doublets, does not clearly exhibit itself in the low-energy Raman spectra (Fig. 3). The CF excitations from the ground state to the remaining two higher-energy states are shown in Fig. 5 at 95 and 239 cm^{-1}. These two transitions are expected to appear in all Raman-active symmetry channels because the two low-lying doublets within the quasiquartet have roughly the same population at 11 K. With the 476.2-nm excitation, the 95-cm^{-1} transition indeed appears as a weak peak for four linear polarizations, while the 239-cm^{-1} transition overlaps with the strong A_{1g} phonon mode. With the 647.1-nm excitation, instead, the 95-cm^{-1} transition becomes weaker, but the 239-cm^{-1} transition is identifiable, manifesting itself as a peak in the RL spectrum and a shoulder in the RR spectrum.

The symmetry of the CF levels is assigned by the following argument: because $YbRh_2Si_2$ and $YbIr_2Si_2$, which have the same lattice structure as $YbRu_2Ge_2$, both have a Γ_6 CF ground state [35,36], we suggest that the CF ground state of $YbRu_2Ge_2$ is also of Γ_6 symmetry (denoted as $\Gamma_6^{(1)}$). The other Kramers doublet within the quasiquartet, in turn, has Γ_7 symmetry (denoted as $\Gamma_7^{(1)}$).

The small difference in the excitation energy measured in the RR and RL geometries near 239 cm^{-1} [Fig. 5(b)] serves as an estimation of the quasiquartet splitting. Using the Lorentzian fits, we find that the excitation energy measured in the RR geometry is higher by 2 ± 1 cm^{-1} than that in the RL geometry at 25 and 15 K. Therefore, the symmetry of the CF state at 239 cm^{-1} is defined to be Γ_6 (denoted as $\Gamma_6^{(2)}$), and the quasiquartet splitting is estimated to be 2 ± 1 cm^{-1}. Because there are only two Γ_6 and two Γ_7 states within the $^2F_{7/2}$ multiplet, the CF state at 95 cm^{-1} can have only Γ_7 symmetry (denoted as $\Gamma_7^{(2)}$).

The energies of the CF excitations at 15 K are summarized in Table II [37].

In an inelastic neutron scattering study of $YbRu_2Ge_2$, excitations at 89, 170, and 260 cm^{-1} were resolved at 5 K with the magnitude of momentum transfer being $\sim$1.9 $\mathrm{Å}^{-1}$ [38]. Their data match well our assignments; the comparison is shown in Table II. This consistency not only supports our assignments but also suggests that the CF excitations and optical phonon modes have little dispersion.

1. Angular electron-cloud distribution of the crystal-field states

We use the following single-ion Hamiltonian to calculate the angular electron-cloud distribution at Yb sites:

$$H = H_{CF} + H_{B_{1g}}. \tag{8}$$

The first term in Eq. (8),

$$H_{CF} = B_2^0\hat{O}_2^0 + B_4^0\hat{O}_4^0 + B_4^4\hat{O}_4^4 + B_6^0\hat{O}_6^0 + B_6^4\hat{O}_6^4, \tag{9}$$

is the general expression for a CF potential of tetragonal site symmetry [39]. The $\hat{O}_2^0$, $\hat{O}_4^0$, $\hat{O}_4^4$, $\hat{O}_6^0$, and $\hat{O}_6^4$ operators are Stevens operators [40]. The five B's are the CF coefficients.

From the CF level diagram, we cannot uniquely determine the CF Hamiltonian and wave functions if we assume tetragonal site symmetry. Hence, we approximate the real tetragonal

CF potential with a dominating cubic CF potential [41] plus a small $\hat{O}_2^0$ axial term:

$$H_{\text{Tetra}} = B_2^0\hat{O}_2^0 + B_4\left(\hat{O}_4^0 + 5\hat{O}_4^4\right) + B_6\left(\hat{O}_6^0 - 21\hat{O}_6^4\right). \quad (10)$$

A cubic CF potential would split the $^2F_{7/2}$ multiplet into one quartet Γ_8 state, one doublet Γ_7 state, and one doublet Γ_6 state of the O_h group. Reducing the cubic symmetry to the tetragonal symmetry, the quartet Γ_8 state of the O_h group would be split into one Γ_7 state and one Γ_6 state of the D_{4h} group. Because $YbRu_2Ge_2$ has a quasiquartet CF ground state, it is possible that this quasiquartet is induced by a small tetragonal perturbation to a large cubic CF potential. This small perturbation is represented by the first term in Eq. (10). We cannot rule out an alternative scenario that the quasiquartet CF ground state of $YbRu_2Ge_2$ has accidental degeneracy, rather than is derived from the quartet Γ_8 state of cubic symmetry. Nevertheless, the Hamiltonian H_{Tetra} preserves the fourfold rotational symmetry along the z axis and is sufficient to provide qualitative insights. In Appendix A we show that based on our assumption, the ratio of $Q_{B_{1g}}$ to $Q_{B_{2g}}$ is calculated to be 1.34, close to the experimentally determined ratio of 1.4 (Sec. III B). This consistency supports our choice of Eq. (10). Experimentally, the wave function of the CF ground state could be determined by core-level nonresonant inelastic x-ray scattering, which has been used for Ce-based heavy-fermion systems [42].

The second term in Eq. (8),

$$H_{B_{1g}} = \frac{V}{2}\left(\hat{J}_x^2 - \hat{J}_y^2\right) = \frac{V}{2}\left(\hat{J}_+^2 + \hat{J}_-^2\right), \quad (11)$$

represents the effective quadrupole-field (QF) potential of B_{1g} symmetry. V measures the strength of the QF potential.

Above T_Q, there is no static B_{1g} QF potential, and we define $H = H_{\text{Tetra}}$. We diagonalize H_{Tetra} in the basis of $|J, m_J\rangle$, where $J = 7/2$ and m_J are the quantum numbers of $\hat{\mathbf{J}}$ and $\hat{J}_z$, respectively. After diagonalization, the CF transition energies can be expressed in terms of B_2^0, B_4, and B_6. We fit the experimentally determined CF level diagram by these three adjustable parameters. There are four sets of parameters which reproduce the level diagram, and we choose the set with the smallest B_2^0 value. The fitting results thus are $B_2^0 = -0.164\,\text{cm}^{-1}$, $B_4 = 0.0518\,\text{cm}^{-1}$, and $B_6 = -0.00442\,\text{cm}^{-1}$. The corresponding angular electron-cloud distribution of the CF states is plotted in Fig. 6.

Below T_Q, there is a finite static B_{1g} QF potential; here we define $H = H_{\text{Tetra}} + H_{B_{1g}}$. We assume that the values of B_2^0, B_4, and B_6 do not change. We diagonalize H in the basis of $|J, m_J\rangle$, and after diagonalization, the CF transition energies can be expressed in terms of V. We find that $V = 0.523\,\text{cm}^{-1}$ renders an additional $2\,\text{cm}^{-1}$ splitting of the ground quartet. In Fig. 7, we plot the angular electron-cloud distribution of the ground quartet for $V = 0.523\,\text{cm}^{-1}$. The charge distribution looks different from the [100] and [010] directions because the $\Gamma_5^{(1)}$ and $\Gamma_5^{(2)}$ doublets carry B_{1g} quadrupole moment. Furthermore, the quadrupole moment carried by the $\Gamma_5^{(1)}$ state and that carried by the $\Gamma_5^{(2)}$ state have approximately the same magnitude but opposite signs [43].

The FQ phase transition reflects the competition between the entropy and energy terms in the Helmholtz free energy

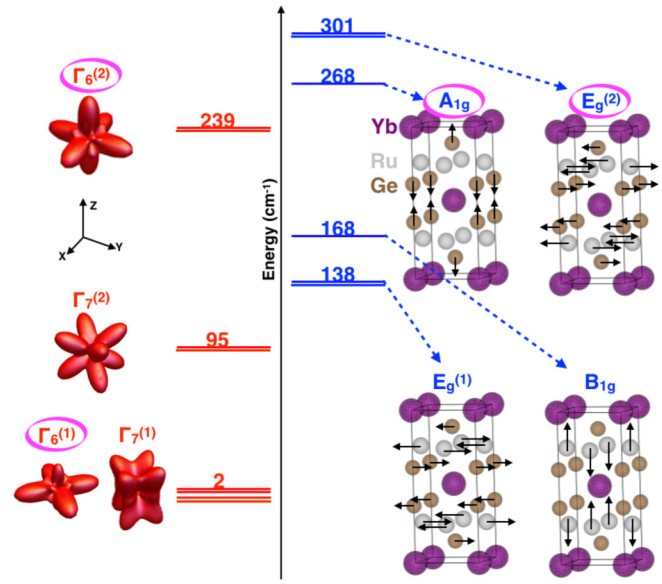

FIG. 6. Schematic energy diagram of the CF states (red horizontal lines) and the phonon modes (blue horizontal lines). The coupled CF transition and phonon modes are circled in purple. On the left are the angular electron-cloud distributions of the four CF states; on the right are the vibration patterns of the phonon modes.

of the system. Above T_Q, the entropy term dominates, and the system prefers a quasidegenerate CF ground state. Below T_Q, instead, the system pursues the lowest possible energy, and an orthorhombic quadrupolar field fulfills the goal: this field mixes the wave functions of the quasidegenerate $\Gamma_6^{(1)}$ and $\Gamma_7^{(1)}$ states, increasing their separation and in turn reducing the ground-state energy. In view of group-theoretical

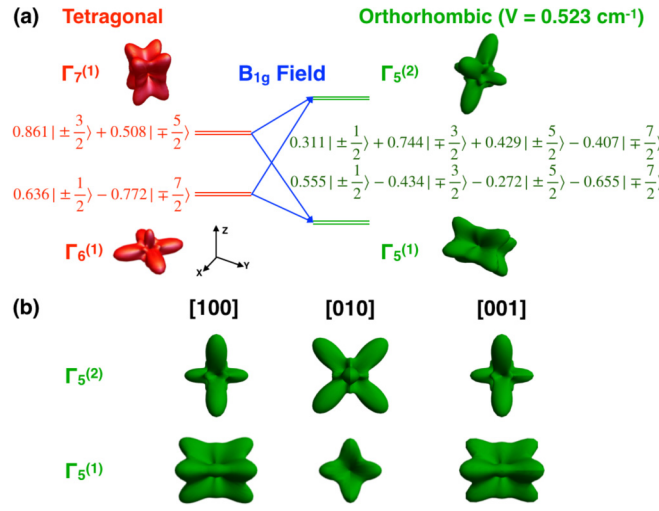

FIG. 7. (a) The effect of the B_{1g} quadrupole-field potential on the ground quasiquartet. The $\Gamma_6^{(1)}$ and $\Gamma_7^{(1)}$ doublets of the D_{4h} group are mixed to form the $\Gamma_5^{(1)}$ and $\Gamma_5^{(2)}$ doublets of the D_{2h} group. The wave functions are expressed in the basis of $|J = 7/2, m_J\rangle$. (b) The angular electron-cloud distribution of the $\Gamma_5^{(1)}$ and $\Gamma_5^{(2)}$ doublets viewed from three orthogonal directions.

considerations, the Γ_6 and Γ_7 irreducible representations of the D_{4h} group become the Γ_5 representation of the D_{2h} group. Correspondingly, the $\Gamma_6^{(1)}$ and $\Gamma_7^{(1)}$ states of the D_{4h} tetragonal phase are mixed by the Hamiltonian $H_{B_{1g}}$ and become the $\Gamma_5^{(1)}$ and $\Gamma_5^{(2)}$ states of the D_{2h} orthorhombic phase.

There are two obvious choices for the macroscopic order parameter of the B_{1g}-symmetry FQ phase. The first is static uniform the quadrupole moment per unit volume:

$$\Psi \propto \left(n_{\Gamma_5^{(1)}} - n_{\Gamma_5^{(2)}}\right) Q_{B_{1g}}, \tag{12}$$

where $n_{\Gamma_5^{(1)}}$ and $n_{\Gamma_5^{(2)}}$ are the occupancies of the $\Gamma_5^{(1)}$ and $\Gamma_5^{(2)}$ states, respectively. The second choice is the lattice orthorhombicity, which couples to the quadrupolar order:

$$\Psi \propto \frac{a-b}{a+b}, \tag{13}$$

where a and b are the in-plane lattice constants. The orthorhombicity as a function of temperature was measured by x-ray diffraction in Ref. [14].

2. *Coupling between the crystal-field transition and the phonon modes*

The coupling between the $\Gamma_6^{(1)} \rightarrow \Gamma_6^{(2)}$ CF transition and the A_{1g} and $E_g^{(2)}$ phonon modes originates from the modulation of the electron-cloud distribution of CF states by lattice vibration (Fig. 6). Such coupling is allowed by group theory because $\Gamma_6 \otimes \Gamma_6 = A_{1g} \oplus A_{2g} \oplus E_g$. We note that the phonon energy and linewidth can be well accounted for by the anharmonic decay model [Figs. 2(a) and 2(b)], suggesting that renormalization due to electron-phonon coupling is small. In the Appendix B we show that for small coupling strength, the temperature dependence of the integrated intensity of the phonon modes $\mathrm{II}(T)$ has the following phenomenological expression:

$$\mathrm{II}(T) = A f_{(1)}(T)[1 - f_{(2)}(T)] + B, \tag{14}$$

where A and B are two constants, $f_{(1)}(T) = 2/Z(T)$ measures the occupancy of the $\Gamma_6^{(1)}$ CF state, and $f_{(2)}(T) = 2e^{-E_4/k_BT}/Z(T)$ measures the occupancy of the $\Gamma_6^{(2)}$ CF state. $Z = 2\sum_{i=1}^{4} e^{-E_i/k_BT}$ is the partition function; $E_1 = 0\,\mathrm{cm}^{-1}$, $E_2 = 2\,\mathrm{cm}^{-1}$, $E_3 = 95\,\mathrm{cm}^{-1}$, and $E_4 = 239\,\mathrm{cm}^{-1}$ are the energies of the CF levels (Table II).

In Eq. (14), the constant B represents the temperature-independent spectral weight of the phonon mode. Without the interaction v and in the absence of a phase transition, the integrated intensity of the phonon modes is expected to be temperature independent. The first term, which is temperature dependent, can be interpreted as the spectral weight transferred from the CF mode to the phonon mode. This transferred spectral weight is proportional to the occupancy of the ground CF state $\Gamma_6^{(1)}$ and the unoccupancy of the excited CF state $\Gamma_6^{(2)}$. The constant A is a measure of the transferred spectral weight at zero temperature [44].

Because of the phase transition at $T_Q = 10\,\mathrm{K}$, Eq. (14) is valid only above 10 K. In addition, group theory allows the $\Gamma_7^{(1)} \rightarrow \Gamma_6^{(2)}$ CF mode to couple to the $E_g^{(2)}$ phonon mode, which is not considered by the simplified equation (14). Because the splitting between the $\Gamma_6^{(1)}$ and $\Gamma_7^{(1)}$ states is only $2\,\mathrm{cm}^{-1}$, including the contribution from the $\Gamma_7^{(1)} \rightarrow \Gamma_6^{(2)}$ CF mode will influence only the fitting curve at a temperature much lower than T_Q, a temperature range where Eq. (14) is invalid.

We use Eq. (14) to fit the phonon intensity data above 10 K in Fig. 2(c). For the A_{1g} phonon mode, $A = 3.14 \pm 0.08$, and $B = 0.06 \pm 0.03$; for the $E_g^{(2)}$ phonon mode, $A = 2.08 \pm 0.05$, and $B = 0.35 \pm 0.02$. These values show that at low temperature, the integrated intensity of the A_{1g} and $E_g^{(2)}$ modes is mainly contributed by the transferred spectral weight. The fitting curves match the data well, which further supports our CF level scheme.

IV. CONCLUSION

In summary, the Raman scattering study of $YbRu_2Ge_2$ focuses on the origin of the ferroquadrupolar transition, as well as on the spectroscopy of phonons and CF excitations within the $^2F_{7/2}$ ground multiplet of Yb^{3+} ion.

The deduced CF level scheme verifies the proposed quasi-quartet ground state, and we estimate that the splitting between two quasidegenerate Kramers doublets is about $2\,\mathrm{cm}^{-1}$. The static electronic Raman susceptibilities in both the B_{1g} and B_{2g} quadrupole channels essentially exhibit Curie law, signifying relatively strong coupling to the lattice in the B_{1g}-symmetry channel that enhances the vanishingly small electronic Weiss temperature to the temperature of quadrupole phase transition at 10 K.

The temperature dependence of the energy and FWHM of the observed phonon modes are described by the anharmonic decay model. The integrated intensities of the A_{1g} and $E_g^{(2)}$ phonon modes show more than 50% enhancement on cooling, which is explained by strong coupling between these phonons and the CF transitions with similar energies.

ACKNOWLEDGMENTS

We thank K. Haule and G. Khanal for discussions. The spectroscopic work at Rutgers (M.Y. and G.B.) was supported by NSF Grant No. DMR-1709161. The work at Stanford (E.W.R. and I.R.F.), including the crystal growth and characterization, was supported by the Gordon and Betty Moore Foundation Emergent Phenomena in Quantum Systems Initiative through Grant No. GBMF4414. G.B. also acknowledges the QuantEmX grant from ICAM and the Gordon and Betty Moore Foundation through Grant No. GBMF5305, which allowed G.B. to make a collaborative visit to Stanford. Work at NICBP was supported by IUT23-3 grant.

APPENDIX A: THE EFFECT OF THE B_{2g} QUADRUPOLE-FIELD POTENTIAL

For completeness, we analyze here the effect of the B_{2g} QF potential on the ground quasiquartet. Following the treatment in Sec. III C 1, we take $H = H_{\mathrm{Tetra}} + H_{B_{2g}}$, where [45]

$$H_{B_{2g}} = \frac{V^*}{2}(\hat{J}_x\hat{J}_y + \hat{J}_y\hat{J}_x) = \frac{V^*}{4i}(\hat{J}_+^2 - \hat{J}_-^2). \tag{A1}$$

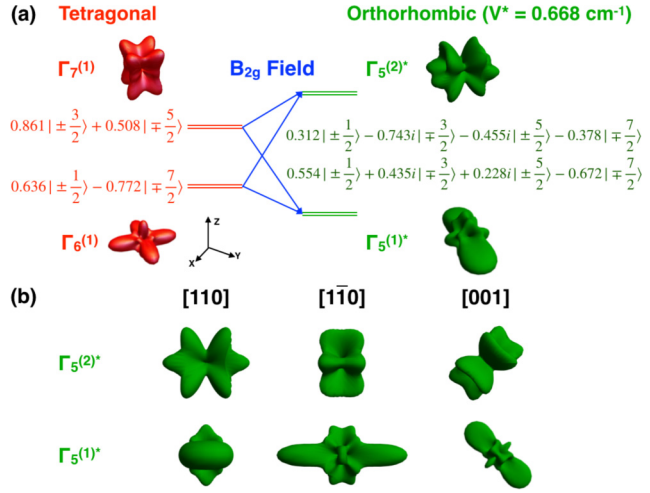

FIG. 8. (a) The effect of the B_{2g} quadrupole-field potential on the ground quasiquartet. The $\Gamma_6^{(1)}$ and $\Gamma_7^{(1)}$ doublets of the D_{4h} group are mixed to form the $\Gamma_5^{(1)*}$ and $\Gamma_5^{(2)*}$ doublets of the D_{2h} group. The wave functions are expressed in the basis of $|J = 7/2, m_J\rangle$. (b) The angular electron-cloud distribution of the $\Gamma_5^{(1)*}$ and $\Gamma_5^{(2)*}$ doublets viewed from three orthogonal directions.

We find that for the B_{2g} potential, $V^* = 0.668\,\mathrm{cm}^{-1}$ renders a 2-cm^{-1} additional splitting of the ground quartet. On the contrary, for the B_{1g} potential $V = 0.523\,\mathrm{cm}^{-1}$ renders a 2-cm^{-1} additional splitting of the ground quartet. Hence, a smaller B_{1g} QF potential is needed to induce the same additional splitting of the quasiquartet. This result is consistent with the conclusion that the coupling between the local quadrupole moments and the lattice strain field is stronger in the B_{1g} channel than in the B_{2g} channel.

In Fig. 8, we plot the angular electron-cloud distribution of the ground quartet for $V^* = 0.668\,\mathrm{cm}^{-1}$. The charge distribution looks different from the [110] and [1$\bar{1}$0] directions because the $\Gamma_5^{(1)*}$ and $\Gamma_5^{(2)*}$ doublets carry B_{2g} quadrupole moment.

The traceless tensor of the electric quadrupole moments [46], written in Cartesian coordinates with arbitrary units, for the $\Gamma_5^{(1)}$ wave function generated by the B_{1g} field, Eq. (11), has the following values:

$$\begin{pmatrix} 0.655 & 0 & 0 \\ 0 & -0.346 & 0 \\ 0 & 0 & -0.309 \end{pmatrix} \tag{A2}$$

Hence, the magnitude of the B_{1g}-symmetry electric quadrupole moment $Q_{B_{1g}}$ of the charge distribution of the $\Gamma_5^{(1)}$ wave function has a value of 1.00 when $V = 0.523\,\mathrm{cm}^{-1}$.

The same tensor for the $\Gamma_5^{(1)*}$ wave function generated by the B_{2g} field, Eq. (A1), has the following values:

$$\begin{pmatrix} 0.176 & -0.748 & 0 \\ -0.748 & 0.176 & 0 \\ 0 & 0 & -0.352 \end{pmatrix}. \tag{A3}$$

The magnitude of the B_{2g}-symmetry electric quadrupole moment $Q_{B_{2g}}$ of the charge distribution of the $\Gamma_5^{(1)*}$ wave function is 0.748 when $V^* = 0.668\,\mathrm{cm}^{-1}$.

Therefore, for the same additional splitting of the ground quasiquartet, the calculated ratio of $Q_{B_{1g}}$ to $Q_{B_{2g}}$ is 1.34. We recall that the experimentally determined ratio of $Q_{B_{1g}}$ to $Q_{B_{2g}}$ is 1.4. This consistency supports the assumptions made in Eq. (10) and shows that the wave functions we use are close to the real wave functions.

APPENDIX B: DERIVATION OF EQUATION (14)

The Hamiltonian of the coupled CF transition and phonon mode can be written in second-quantization form as

$$H = \omega_1 \hat{a}_1^\dagger \hat{a}_1 + \omega_2 \hat{a}_2^\dagger \hat{a}_2 + \omega_p \hat{b}^\dagger \hat{b} + v(\hat{a}_2^\dagger \hat{a}_1 - \hat{a}_1^\dagger \hat{a}_2)(\hat{b}^\dagger + \hat{b}), \tag{B1}$$

where $\hat{a}^\dagger$ and $\hat{a}$ are fermionic creation and destruction operators and $\hat{b}^\dagger$ and $\hat{b}$ are bosonic creation and destruction operators. The first and second terms describe, respectively, the energy of the lower and upper CF levels; the third term is the phonon energy, and the last term is the coupling between the CF transition and the phonon mode. The coefficient v measures the strength of the coupling, which we take as a real number.

The CF transition corresponds to a bubble-shaped Feynman diagram of the electron-hole pair. Neglecting self-energy, the propagator has the following form:

$$P(\omega, T) = \frac{f_1(T)[1 - f_2(T)]}{\omega - (\omega_e - i\epsilon)} - \frac{[1 - f_1(T)]f_2(T)}{\omega + (\omega_e + i\epsilon)}, \tag{B2}$$

where $f_1(T)$ and $f_2(T)$ are, respectively, the temperature-dependent occupancy of the lower and upper CF levels; $\omega_e = \omega_2 - \omega_1$ is the energy of the CF transition, and ϵ is an infinitesimal positive value.

The phonon propagator is

$$D(\omega, T) = \frac{1 + n(\omega_p, T)}{\omega - (\omega_p - i\epsilon)} - \frac{n(\omega_p, T)}{\omega + (\omega_p + i\epsilon)}, \tag{B3}$$

where $n(\omega_p, T)$ is the Bose distribution function.

The experimentally measured scattering rate $I(\omega, T)$ has the form

$$I(\omega, T) \sim \frac{1}{\pi} \mathrm{Im} T^\dagger G(\omega, T) T, \tag{B4}$$

where $T^\dagger = (T_p\ T_e)$ is the vertex of the light scattering and $G(\omega, T)$ is the Green's function of the Hamiltonian in Eq. (B1). G can be obtained by solving the Dyson equation:

$$G(\omega, T) = \frac{1}{1 - P(\omega, T) v D(\omega, T) v} \times \begin{pmatrix} D(\omega, T) & D(\omega, T) v P(\omega, T) \\ P(\omega, T) v D(\omega, T) & P(\omega, T) \end{pmatrix}. \tag{B5}$$

In the following derivation, we assume v is small so that the prefactor in the above expression can be replaced by unity.

Then the approximated form of $I(\omega, T)$ is

$$\frac{1}{\pi}\mathrm{Im}[T_p^2 D(\omega, T) + 2T_p T_e D(\omega, T) v P(\omega, T) + T_e^2 P(\omega, T)]. \tag{B6}$$

By virtue of Sokhotsky's formula

$$\lim_{\epsilon \to 0^+} \frac{1}{\omega \pm (\omega_0 - i\epsilon)} = \mathrm{p.v.}\frac{1}{\omega \pm \omega_0} \pm i\pi\delta(\omega \pm \omega_0), \tag{B7}$$

where p.v. stands for the principle value, we derive from Eq. (B6) the Stokes part of the scattering rate:

$$I(\omega, T) \sim T_p^2[1 + n(\omega_p, T)]\delta(\omega - \omega_p) + T_e^2 f_1(T)[1 - f_2(T)]\delta(\omega - \omega_e) + 2T_p T_e v[1 + n(\omega_p, T)]f_1(T)[1 - f_2(T)] \times \left[\frac{\delta(\omega - \omega_p)}{\omega_p - \omega_e} + \frac{\delta(\omega - \omega_e)}{\omega_e - \omega_p}\right]. \tag{B8}$$

Therefore, the phonon scattering rate $I_p(\omega, T)$ is

$$I_p(\omega, T) \sim T_p^2[1 + n(\omega_p, T)]\delta(\omega - \omega_p) + 2T_p T_e v[1 + n(\omega_p, T)]f_1(T)[1 - f_2(T)]\frac{\delta(\omega - \omega_p)}{\omega_p - \omega_e}, \tag{B9}$$

which can be arranged into

$$T_p^2[1 + n(\omega_p, T)]\left\{1 + 2\frac{T_e}{T_p}\frac{v}{\omega_p - \omega_e}f_1(T)[1 - f_2(T)]\right\}\delta(\omega - \omega_p). \tag{B10}$$

The phonon response function $\chi_p''(\omega, T)$, in turn, is

$$\chi_p''(\omega, T) \sim T_p^2\left\{1 + 2\frac{T_e}{T_p}\frac{v}{\omega_p - \omega_e}f_1(T)[1 - f_2(T)]\right\}\delta(\omega - \omega_p), \tag{B11}$$

and integration of $\chi_p''(\omega, T)$ yields the integrated intensity of the phonon mode $\mathrm{II}(T)$:

$$\mathrm{II}(T) \sim T_p^2\left\{1 + 2\frac{T_e}{T_p}\frac{v}{\omega_p - \omega_e}f_1(T)[1 - f_2(T)]\right\}. \tag{B12}$$

Equation (B12) can be cast in a phenomenological form:

$$\mathrm{II}(T) = A f_1(T)[1 - f_2(T)] + B, \tag{B13}$$

where $A \sim \frac{T_e T_p v}{\omega_p - \omega_e}$ and $B \sim T_p^2$ are two constants. Equation (B13) is the same as Eq. (14) used in the main text to fit the experimentally measured temperature dependence of the integrated intensity of the A_{1g} and $E_g^{(2)}$ phonon modes.

[1] Y. Kuramoto, H. Kusunose, and A. Kiss, Multipole orders and fluctuations in strongly correlated electron systems, J. Phys. Soc. Jpn. **78**, 072001 (2009).

[2] P. Santini, S. Carretta, G. Amoretti, R. Caciuffo, N. Magnani, and G. H. Lander, Multipolar interactions in f-electron systems: The paradigm of actinide dioxides, Rev. Mod. Phys. **81**, 807 (2009).

[3] J.-M. Mignot, I. N. Goncharenko, P. Link, T. Matsumura, A. Gukasov, and T. Suzuki, Neutron-diffraction study of magnetic and quadrupolar order in Tm monochalcogenides, Phys. B (Amsterdam, Neth.) **276**, 756 (2000).

[4] K. Hirota, N. Oumi, T. Matsumura, H. Nakao, Y. Wakabayashi, Y. Murakami, and Y. Endoh, Direct Observation of Antiferroquadrupolar Ordering: Resonant X-Ray Scattering Study of DyB_2C_2, Phys. Rev. Lett. **84**, 2706 (2000).

[5] J. A. Paixão, C. Detlefs, M. J. Longfield, R. Caciuffo, P. Santini, N. Bernhoeft, J. Rebizant, and G. H. Lander, Triple-$\vec{q}$ Octupolar Ordering in NpO_2, Phys. Rev. Lett. **89**, 187202 (2002).

[6] K. Kuwahara, K. Iwasa, M. Kohgi, K. Kaneko, N. Metoki, S. Raymond, M.-A. Méasson, J. Flouquet, H. Sugawara, Y. Aoki, and H. Sato, Inelastic neutron scattering study on low-energy excitations of the heavy-fermion superconductor $PrOs_4Sb_{12}$, Phys. B (Amsterdam, Neth.) **385–386**, 82 (2006).

[7] A. S. Cameron, G. Friemel, and D. S. Inosov, Multipolar phases and magnetically hidden order: Review of the heavy-fermion compound $Ce_{1-x}La_xB_6$, Rep. Prog. Phys. **79**, 066502 (2016).

[8] H. S. Jeevan, C. Geibel, and Z. Hossain, Quasiquartet crystal-electric-field ground state with possible quadrupolar ordering in the tetragonal compound $YbRu_2Ge_2$, Phys. Rev. B **73**, 020407(R) (2006).

[9] T. Takimoto and P. Thalmeier, Theory of induced quadrupolar order in tetragonal $YbRu_2Ge_2$, Phys. Rev. B **77**, 045105 (2008).

[10] P. Thalmeier, T. Takimoto, J. Chang, and I. Eremin, Multipolar order and superconductivity in f-electron compounds, J. Phys. Soc. Jpn. **77**, 43 (2008).

[11] M. Nicklas, M. E. Macovei, H. S. Jeevan, C. Geibel, and Z. Hossain, Pressure dependence of the magnetic and quadrupolar ordering in $YbRu_2Ge_2$, J. Low Temp. Phys. **159**, 151 (2010).

[12] A. Prasad, H. S. Jeevan, C. Geibel, and Z. Hossain, Suppression of quadrupolar order on Si doping in $YbRu_2(Ge_{1-x}Si_x)_2$, J. Phys.: Condens. Matter **22**, 126004 (2010).

[13] H. S. Jeevan, D. T. Adroja, A. D. Hillier, Z. Hossain, C. Ritter, and C. Geibel, Muon spin relaxation and neutron diffraction investigations of quadrupolar and magnetically ordered states of $YbRu_2Ge_2$, Phys. Rev. B **84**, 184405 (2011).

[14] E. W. Rosenberg, J.-H. Chu, J. P. C. Ruff, A. T. Hristov, and I. R. Fisher, Divergence of the quadrupole-strain susceptibility of the electronic nematic system $YbRu_2Ge_2$, Proc. Natl. Acad. Sci. USA **116**, 7232 (2019).

[15] H. Pfau, E. W. Rosenberg, P. Massat, B. Moritz, M. Hashimoto, D. Lu, I. R. Fisher, and Z.-X. Shen, Electronic structure of the quadrupolar ordered heavy-fermion compound $YbRu_2Ge_2$ measured by angle-resolved photoemission, Phys. Rev. B **99**, 075159 (2019).

[16] M. Kosaka, H. Onodera, K. Ohoyama, M. Ohashi, Y. Yamaguchi, S. Nakamura, T. Goto, H. Kobayashi, and S. Ikeda, Quadrupolar ordering and magnetic properties of tetragonal $TmAu_2$, Phys. Rev. B **58**, 6339 (1998).

[17] M. V. Klein, Raman Studies of Phonon Anomalies in Transition-Metal Compounds, in *Light Scattering in Solids III*, edited by M. Cardona and G. Güntherodt (Springer, Berlin, 1982), pp. 128–178.

[18] G. Schaack, Raman scattering by crystal-field excitations, in *Light Scattering in Solids VII*, edited by M. Cardona and G. Güntherodt (Springer, Berlin, 2000), pp. 30–179.

[19] Optical absorption coefficient and thermal conductivity data for $YbRu_2Ge_2$, which are required for a model estimation of the laser heating [47], are currently unavailable. Hence, we base the estimate of laser heating at low temperatures on a comparison with other heavy-fermion metals with comparable electrical conductivity [14]: CeB_6 [48] and URu_2Si_2 [49], for which laser heating for the same experimental setup was established in the range of 0.5–1.0 K/mW.

[20] W. Hayes and R. Loudon, *Scattering of Light by Crystals* (John Wiley and Sons, New York, 1978).

[21] P. G. Klemens, Anharmonic decay of optical phonons, Phys. Rev. **148**, 845 (1966).

[22] J. Menéndez and M. Cardona, Temperature dependence of the first-order Raman scattering by phonons in Si, Ge, and $\alpha - Sn$: Anharmonic effects, Phys. Rev. B **29**, 2051 (1984).

[23] S. L. Cooper, M. V. Klein, M. B. Maple, and M. S. Torikachvili, Magnetic excitations and phonon anomalies in URu_2Si_2, Phys. Rev. B **36**, 5743(R) (1987).

[24] W.-L. Zhang, A. S. Sefat, H. Ding, P. Richard, and G. Blumberg, Stress-induced nematicity in $EuFe_2As_2$ studied by Raman spectroscopy, Phys. Rev. B **94**, 014513 (2016).

[25] A detailed discussion of the symmetry breaking and the wave function mixing can be found in Sec. III C.

[26] V. K. Thorsmølle, M. Khodas, Z. P. Yin, Chenglin Zhang, S. V. Carr, P. Dai, and G. Blumberg, Critical quadrupole fluctuations and collective modes in iron pnictide superconductors, Phys. Rev. B **93**, 054515 (2016).

[27] Y. Gallais and I. Paul, Charge nematicity and electronic raman scattering in iron-based superconductors, C. R. Phys. **17**, 113 (2016).

[28] We note that in the elastoresistivity studies, the Weiss temperature obtained from a fit to the static quadrupole-strain susceptibility is also a measure of an extrapolated bare electronic quadrupolar transition temperature because of the clamped lattice [14]. This is the reason why the Weiss temperatures extrapolated from the Raman susceptibility and from quadrupole-strain susceptibility agree.

[29] J. H. Van Vleck, Note on the interactions between the spins of magnetic ions or nuclei in metals, Rev. Mod. Phys. **34**, 681 (1962), and references therein.

[30] M. Bouvier, G. L. F. Fraga, A. Garnier, D. Gignoux, D. Schmitt, and T. Shigeoka, Anomalous low-temperature magnetic behaviour in $DyRu_2Si_2$ and $DyRu_2Ge_2$, Europhys. Lett. **33**, 647 (1996).

[31] A. E. Böhmer, T. Arai, F. Hardy, T. Hattori, T. Iye, T. Wolf, H. v. Löhneysen, K. Ishida, and C. Meingast, Origin of the Tetragonal-to-Orthorhombic Phase Transition in FeSe: A Combined Thermodynamic and NMR Study of Nematicity, Phys. Rev. Lett. **114**, 027001 (2015).

[32] A. E. Böhmer and C. Meingast, Electronic nematic susceptibility of iron-based superconductors, C. R. Phys. **17**, 90 (2016).

[33] K. Mitsumoto, S. Goto, Y. Nemoto, M. Akatsu, T. Goto, N. D. Dung, T. D. Matsuda, Y. Haga, T. Takeuchi, K. Sugiyama, R. Settai, and Y. Ōnuki, Quadrupole effects in tetragonal crystals $PrCu_2Si_2$ and $DyCu_2Si_2$, J. Phys. Condens. Matter **25**, 296002 (2013).

[34] G. F. Koster, *Properties of the Thirty-Two Point Groups* (MIT Press, Cambridge, MA, 1963).

[35] A. S. Kutuzov and A. M. Skvortsova, Crystal electric field parameters for Yb^{3+} ion in $YbRh_2Si_2$, J. Phys.: Conf. Ser. **324**, 012039 (2011).

[36] A. M. Leushin and V. A. Ivanshin, Crystalline electric fields and the ground state of $YbRh_2Si_2$ and $YbIr_2Si_2$, Phys. B (Amsterdam, Neth.) **403**, 1265 (2008).

[37] We note that if the CF ground state had Γ_7 symmetry, the symmetry of the CF states at 2, 95, and 239 cm^{-1} would instead be Γ_6, Γ_6, and Γ_7, respectively.

[38] H. S. Jeevan, Crystal growth and investigation of $CeCu_2Si_2$ and $YbRu_2Ge_2$: Competition/Co-existence of superconducting, dipolar and quadrupolar order, Ph.D. thesis, Max Planck Institute for Chemical Physic of Solids, Dresden, 2010.

[39] G. Fischer and A. Herr, Representation of energetical and low-field magnetic properties of $j = 5/2$ rare earth ion states in tetragonal crystal fields, Phys. Status Solidi B **141**, 589 (1987).

[40] K. W. H. Stevens, Matrix elements and operator equivalents connected with the magnetic properties of rare earth ions, Proc. Phys. Soc. A **65**, 209 (1952).

[41] K. R. Lea, M. J. M. Leask, and W. P. Wolf, The raising of angular momentum degeneracy of f-electron terms by cubic crystal fields, J. Phys. Chem. Solids **23**, 1381 (1962).

[42] M. Sundermann, A. Amorese, F. Strigari, M. W. Haverkort, L. H. Tjeng, M. Moretti Sala, H. Yavş, E. D. Bauer, P. F. S. Rosa, J. D. Thompson, and A. Severing, Orientation of ground-state orbital in $CeCoIn_5$ and $CeRhIn_5$, arXiv:1902.06726.

[43] Strictly speaking, the quadrupole moments have the same magnitude only if we ignore the contribution by higher-energy CF states.

[44] We note that there is no general sum rule for Raman spectroscopy.

[45] Asterisks are used to distinguish the symbols used for $H_{B_{2g}}$ from those used for $H_{B_{1g}}$.

[46] J. David Jackson, Multipoles, electrostatics of macroscopic media, dielectrics, in *Classical Electrodynamics* (Wiley, New York, 1999), pp. 145–173.

[47] A. A. Maksimov, A. V. Puchkov, I. I. Tartakovskii, V. B. Timofeev, D. Reznik, and M. V. Klein, Investigations of the temperature dependence of the low energy electronic Raman scattering in $Tl_2Ba_2CaCu_2O_8$ single crystals, Solid State Commun. **81**, 407 (1992).

[48] A. Takase, K. Kojima, T. Komatsubara, and T. Kasuya, Electrical resistivity and magnetoresistance of CeB_6, Solid State Commun. **36**, 461 (1980).

[49] T. T. M. Palstra, A. A. Menovsky, and J. A. Mydosh, Anisotropic electrical resistivity of the magnetic heavy-fermion superconductor URu_2Si_2, Phys. Rev. B **33**, 6527(R) (1986).